Chemical Engineering Science 66 (2011) 1866–1878

Contents lists available at ScienceDirect

Chemical Engineering Science

journal homepage: www.elsevier.com/locate/ces

Kinetics of fluidized bed spray agglomeration for compact and porous particles

Korina Terrazas-Velarde *, Mirko Peglow, Evangelos Tsotsas

Thermal Process Engineering, Otto von Guericke University, Universitätsplatz 2, 39106 Magdeburg, Germany

ARTICLE INFO

Article history:
Received 4 June 2010
Received in revised form
14 January 2011
Accepted 20 January 2011

Keywords:
Agglomeration
Fluidization
Mathematical modeling
Particle formation
Droplet penetration
Particle porosity

ABSTRACT

The effect of the primary particle porosity during the formation of agglomerates in spray fluidized beds is presented in this study. The method is based on the single micro-interactions occurring within the fluidized bed such as inter-particle collisions, droplet spread on the particle surface, aging of the deposited droplets and particle coalescence. The porous character of the particles is expected to directly affect the aging process of the deposited binder layer by penetration into the pores of the substrate. The droplet penetration process is experimentally analyzed by single droplet deposition on spherical, porous alumina particles. The results indicate that the penetration process is mainly governed by the viscosity of the liquid and that at relatively low viscosities, droplet penetration is fast. For highly viscous liquids, the penetration velocity slows down and an additional mechanism, namely drying becomes important. A combined imbibition–drying model is developed and included into a comprehensive stochastic agglomeration model that allows the simulation of agglomerate formation in a batch process. Lab-scale agglomeration experiments with porous and non-porous particles are carried out in an attempt to validate the general tendencies predicted by the main agglomeration model. The results show that the agglomeration rate for porous particles is significantly reduced due to the losses of deposited droplets into the pores of the primary particles; this tendency is much more pronounced at low binder viscosities.

1. Introduction

Size enlargement processes have the purpose of changing the physical properties of powders in order to meet desired product specifications such as size, shape, flowability, density, solubility or porosity (Ennis, 1996). Agglomeration achieves size enlargement by combining small particles to larger entities (Couper et al., 2010). This is commonly done by dispersing liquid binders onto the powder bed and forming interparticulate bonds. One of the most successfully applied devices is the fluidized bed spray agglomerator. The most significant advantage of this apparatus is that it allows the combination of binder dispersion and drying in a single process (Litster and Ennis, 2004). However, the complexity of the hydrodynamics of fluidized systems combined with the study of agglomeration, breakage and drying kinetics makes the process relatively difficult to describe. The mathematical description of a system of particles undergoing agglomeration is usually done by population balances (Kumar et al., 2008). Although this approach has been successfully applied, it shows several drawbacks such as the uncertainties of choosing among many available agglomeration or rupture kernels, the complexity of numerical solutions and the limited capability of introducing several processes simultaneously. These disadvantages can be overcome by the use of stochastic methods (Zaho et al., 2007). The micro-level stochastic modeling of agglomeration processes has been applied by several researchers demonstrating that the stochastic solution is able to describe the size enlargement process in a straightforward manner. Recent publications have focused on the use of this approach to analyze the effect of process parameters such as binder addition rate, binder viscosity, fluidization velocity or liquid–solid contact angle on agglomeration kinetics of non-porous particles (Thielmann et al., 2008; Terrazas-Velarde et al., 2009). However, the intraparticle porosity of the primary particles may lead to a significantly different agglomeration behavior. The present work deals with the effect of the porous nature of substrates on agglomerate formation. The study is based on the stochastic approach presented by Terrazas-Velarde et al. (2009) with proper extensions to the model in order to include droplet imbibition into the porous particles (in this work the term "imbibition" is used as synonym for droplet penetration or absorption). Additionally, experiments at micro-level scale are compared with the model of droplet penetration into the pores of the particles and lab-scale experiments are carried out in an attempt to validate the agglomeration model.

* Corresponding author. Tel.: +49 391 67 18267; fax: +49 391 67 11160.
E-mail address: korinaterrazas@yahoo.com.mx (K. Terrazas-Velarde).

0009-2509/$ - see front matter © 2011 Elsevier Ltd. All rights reserved.
doi:10.1016/j.ces.2011.01.037

2. Computational method

2.1. General algorithm

The micro-level investigation of agglomeration kinetics involves the study of several mechanisms happening within the apparatus such as droplet capture, particle wetting, deposited droplet drying, particle collisions or liquid bridge formation and solidification. As suggested by several authors, the droplet capture mechanism is the rate determining step during agglomeration (Tan et al., 2006). The droplet addition rate is directly related to the binder mass flow rate, droplet and particle diameters and the initial bed mass or the number of primary particles in the bed as follows:

$$\gamma = \frac{\dot{M}_l}{M_{bed}} \left(\frac{\rho_p}{\rho_l}\right) \left(\frac{d_p}{d_d}\right)^3. \tag{1}$$

This quantity represents the number of droplets per primary particle per second that are sprayed onto the powder bed and should be equal for the real and simulated fluidized bed. As overspray or premature droplet solidification is not accounted for, γ also represents the droplet capture rate.

Once the particle captures a droplet, this droplet spreads on the particle surface and, depending on several parameters such as droplet impact velocity, liquid viscosity or surface tension, it takes its equilibrium shape. The present study assumes that the equilibrium shape is reached immediately after deposition and that the deposited radius a and height h_0 can be calculated by the so-called two parameter model equations (Clarke et al., 2002)

$$a = \left(\frac{3V_d}{\pi} \frac{\sin^3\theta}{2-3\cos\theta+\cos^3\theta}\right)^{1/3} \tag{2}$$

and

$$h_0 = a\left(\frac{1-\cos\theta}{\sin\theta}\right). \tag{3}$$

The porous or non-porous character of the particles is not expected to affect either the rate of droplet capture γ or the initial binder height h_0 as these parameters depend only on droplet and particle diameters as well as solid–liquid contact angle. However, once the droplet is deposited, the porosity of the particles plays a major role in the droplet availability for a successful collision. In non-porous particle systems, deposited droplets that have not been consumed to form a liquid bridge undergo height reduction only by drying. On the contrary, in porous particle systems the droplets not only dry but also penetrate the particles, reducing the droplet availability in the system and presumably decreasing the agglomeration efficiency.

In order to correlate the real with the computational time, the following empirical correlation which describes the number of collisions that a single particle experiences per second is used (Buffière and Moletta, 2000)

$$f_{coll} = F_{coll}\left[1-\left(\frac{\phi_{exp}}{\phi_{fix}}\right)\right]\left(\frac{\phi_{exp}}{\phi_{fix}}\right)^2 u_0, \tag{4}$$

where f_{coll} is the collision frequency in 1/s, u_0 is the fluidization velocity in m/s, ϕ_{exp} and ϕ_{fix} are the solid volume fractions of the expanded and the fixed bed, and F_{coll} is the collision frequency pre-factor. In the work of Buffière and Moletta (2000), this parameter was adjusted to $F_{coll}=56{,}400$ on the basis of experiments in aerated liquid-fluidized beds. However, F_{coll} can be readjusted to describe the collision behavior of any particle population. In the present work, Eq. (4) was applied by adjusting F_{coll} for a single "base-case" simulation to the corresponding experimental results. In this way, an estimate of the number of collisions per particle per second which is characteristic for the investigated particulate system was indirectly accomplished. Then, this value of F_{coll} was used for every simulation of the same particulate system. It is presumed that the obtained f_{coll} represents the collision frequency which becomes efficient in the sense of agglomeration (Terrazas-Velarde et al., in press).

The solution method follows an event-driven scheme with periodical particle regulation, the so-called Constant Volume Monte Carlo method. The entire particle population, consisting of N_p particles, is divided into two randomly chosen groups of equal size. When the number of particles is odd then the last particle of Group A does not collide in this particular collision. Due to the high number of particles and collisions, the non-collision of a single particle is not expected to have a big influence on the simulation. Furthermore, in reality, it is also possible that not all collisions take place between particles, e.g., particle–wall collisions which does not produce any coalescence. The selection of the colliding pair of particles is independent on particle properties. An event k is defined as the pairwise collisions between all particles of the two groups. The number of desired events k is given at the beginning of the simulation and each event corresponds to $i=N_p/2$ pairwise collisions. Each collision i is monitored in order to determine whether agglomeration or rebound takes place. Once the number of pairs i has finished in k, the new properties of the particle population are determined and the length of the actual time step is set to

$$t_{step} = \frac{1}{f_{coll}}. \tag{5}$$

Then, the next two groups of particles are chosen for the event $k+1$ until $k+1=k_{end}$. The elapsed real time is calculated as

$$t_{real} = \sum_{k=1}^{k_{end}} t_{step}. \tag{6}$$

The well known Stokes criterion is used for the description of agglomeration-rebound events (Ennis et al., 1991). A pair of colliding particles is assumed to coalesce when their Stokes number St_{coal} described by

$$St_{coal} = \frac{2M_{agg}u_c}{3\pi\mu_l {d_{agg}}^2} \tag{7}$$

is smaller than the critical Stokes number St^*_{coal} given by

$$St^*_{coal} = \left(1+\frac{1}{e}\right)\ln\left(\frac{h}{h_a}\right). \tag{8}$$

Here the average agglomerate M_{agg} mass and diameter d_{agg}, respectively, are

$$M_{agg} = \frac{2M_{agg1}M_{agg2}}{M_{agg1}+M_{agg2}}, \tag{9}$$

$$d_{agg} = \frac{2d_{agg1}d_{agg2}}{d_{agg1}+d_{agg2}}. \tag{10}$$

That means Eqs. (7)–(10) are applied to each sub-collision i (assuming than the particles contact each other in a wet position). For the concept of positions which give the assumed agglomerate structure as well as further details on the method please refer to Terrazas-Velarde et al. (2009) and Terrazas-Velarde (2010). Regarding the collision velocity included in Eq. (7), it is assumed to be independent of the agglomerate mass and directly related to bed turbulence and to the superficial gas velocity u_0 (George et al., 2008). Then, the collision velocity of the pair of particles u_c is randomly chosen, assuming a normally distributed function around a mean value equal to $0.5u_0$ with a standard deviation of 0.1 m/s. For the sake of simplicity both values are assumed constant and independent of agglomerate size or agglomerate size

distribution. The relaxation of this assumption certainly represents an area of improvement; a collision velocity based on the granular temperature (Gidaspow, 1994), generally obtained from expensive CFD simulations, may be quantitatively more accurate (Rajniak et al., 2009). However, this is beyond the scope of the present study. Regarding the kind of distribution, and analogous to the kinetic theory of gases, it is widely accepted that the distribution of particle velocities within the fluidized bed may take the form of a normalized, Gaussian curve (Cryer, 1999). The value of the standard deviation was taken based on the order of magnitude of the superficial fluidization velocity. Certainly, the assumptions taken in this respect may be a source of error and represent a limitation to the stochastic methods. However, the simplification adopted here is not expected to affect qualitatively the interactions between the various micro-mechanisms considered.

As it can be seen in Eq. (8), the coalescence limit of the particles is ruled by material properties such as the restitution coefficient e or the height of the surface asperities h_a. Additionally, the deposited layer height h plays a major role in the coalescence process. Immediately after the formation of a spherical cap on the particle surface, the deposited droplet is available to potentially form a liquid bridge and produce coalescence with another particle or agglomerate. However, if no successful coalescence is observed, the deposited droplet ability to dissipate the collision kinetic energy is modified as time advances. Two main mechanisms are responsible for the aging of deposited droplets, namely droplet drying and imbibition into porous substrates. The nature of the solid substrate is crucial and decides which mechanism dominates during height reduction. In non-porous systems, deposited layer reduction and, eventually, the slowing down of agglomeration due to droplet losses are solely attributed to drying of the liquid binder. On the other hand, both mechanisms are present in porous systems.

2.2. Deposited droplet drying

In this study, the reduction of the deposited droplet height only by drying is described by

$$h_{dry} = h_0 - \frac{2}{3}\frac{\rho_g}{\rho_w}\frac{\tilde{M}_w}{\tilde{M}_g}\frac{\beta}{1-\cos\theta}\left(\frac{P_v^*}{P}-\tilde{y}_g\right)\left[\frac{1}{1-\cos\theta}-\frac{1}{3}\right]^{-1} t, \tag{11}$$

where β is the mass transfer coefficient, P_v^* and P are the saturation vapor pressure and the system pressure, respectively. The molar fraction in the gas phase $\tilde{y}_g$ is calculated by assuming that the fluidized bed is a perfectly mixed medium and that the amount of evaporating water is at any time equal to the amount of sprayed water as

$$\tilde{y}_g = \frac{Y_g}{Y_g + (\tilde{M}_w/\tilde{M}_g)}. \tag{12}$$

Then, Eq. (11) describes the reduction of the deposited droplet height with time as a function of temperature, fluidization velocity, contact angle, particle, binder and fluidization gas properties. A discussion on the experimental validation of the model can be found in Terrazas-Velarde et al. (in press).

2.3. Deposited droplet imbibition

The imbibition process is assumed as the liquid penetration into a network of non-interconnected and equisized cylindrical pores as it is schematically depicted in Fig. 1.

Then, the mass of liquid in a cylindrical capillary at any time is given by

$$M_l = \rho_l V_l = \rho_l \pi r^2 y, \tag{13}$$

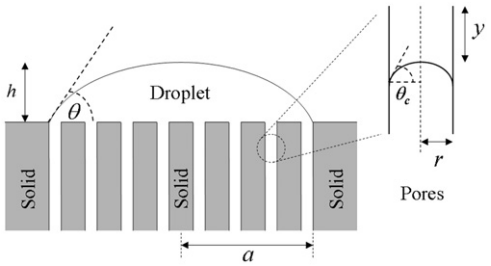

Fig. 1. Schematic representation of the imbibition model.

where r is the capillary radius and y is the vertical distance from the liquid reservoir.

Taking the first derivative of Eq. (13) one obtains the liquid penetration velocity into the capillary as follows:

$$\frac{dM_l}{dt} = \rho_l \pi r^2 \frac{dy}{dt}. \tag{14}$$

Additionally, it applies for the deposited droplet (spherical cap)

$$M_{cap} = \rho_l V_{cap} = \rho_l \pi h^3 \left[\frac{1}{1-\cos\theta}-\frac{1}{3}\right]. \tag{15}$$

Deriving Eq. (15) the following expression for the transient reduction of the liquid layer height is obtained:

$$\frac{dM_{cap}}{dt} = 3\rho_l \pi \left[\frac{1}{1-\cos\theta}-\frac{1}{3}\right] h^2 \frac{dh}{dt}. \tag{16}$$

Considering the solid particle as a matrix of vertically arranged capillaries (pores), the total number of open pores on the wetted surface, is given by

$$N_{pore} = \varepsilon_p \frac{A_{wet}}{A_{pore}} \tag{17}$$

This last equation accounts for the intraparticle porosity ε_p and the ratio between the wet surface area covered by the droplet A_{wet} and the pore cross section area A_{pore}. These characteristic areas can be described by

$$A_{wet} = \pi a^2 = \pi h^2 \left(\frac{\sin\theta}{1-\cos\theta}\right)^2, \tag{18}$$

$$A_{pore} = \pi r_{pore}^2. \tag{19}$$

Combining Eqs. (18) and (19) in Eq. (17) the following relationship for N_{pore} is obtained:

$$N_{pore} = \varepsilon_p \left(\frac{h^2}{r_{pore}^2}\right)\left(\frac{\sin\theta}{1-\cos\theta}\right)^2. \tag{20}$$

Furthermore, the mass being lost in the deposited droplet can be expressed as

$$\frac{dM_{cap}}{dt} = -N_{pore}\frac{dM_l}{dt}. \tag{21}$$

Combining Eqs. (14), (16) and (20), with $r = r_{pore}$ in Eq. (21), the following expression is obtained:

$$\frac{dh}{dy} = -\frac{\varepsilon_p}{3}\left(\frac{\sin\theta}{1-\cos\theta}\right)^2\left[\frac{1}{1-\cos\theta}-\frac{1}{3}\right]^{-1}. \tag{22}$$

Solving Eq. (22) for h, the geometrical relationship between the height of the liquid layer and the penetration distance into the capillaries y can be expressed as

$$y = \frac{3}{\varepsilon_p}\left(\frac{\sin\theta}{1-\cos\theta}\right)^{-2}\left[\frac{1}{1-\cos\theta}-\frac{1}{3}\right](h_0-h). \tag{23}$$

Following the well known Washburn theory (Washburn, 1921; Czachor, 2007), the penetration of a liquid (in this case binder solution) into a capillary of radius r (or radius of the pore r_{pore}) is described by a force balance of the form

$$F_c = F_{gr} + F_v, \tag{24}$$

where F_c, F_{gr} and F_v are the capillary, gravity and viscous forces, respectively, described by

$$F_c = 2\pi r_{pore}\sigma_l \cos\theta_c, \tag{25}$$

$$F_{gr} = \pi\rho_l g r_{pore}^2 y, \tag{26}$$

$$F_v = 8\pi\mu_l y\frac{dy}{dt}. \tag{27}$$

In Eq. (25), θ_c is the internal contact angle within the capillary. As this quantity is not observable and for the sake of simplicity, it is assumed than the contact angle at the surface of the particle is equal to the internal contact angle. An additional assumption of the model refers to the effect of gravity on the imbibition process. It is widely known than capillary and viscous forces act opposite to each other. However, depending on the position of the deposited droplet with respect to the gravity field, the gravity force may accelerate or reduce the penetration velocity. A deposited droplet may be located at the top of the particle with gravity and capillary forces acting in the same direction facilitating in this way the penetration of the liquid into the pore. In the opposite case, when the droplet is located at the bottom, gravity and capillary forces act in opposite directions and imbibition may be slowed down. Due to the permanent rotation of the particles in the fluidized bed, these two cases (top and bottom) as well as any other position of the droplet with respect to the direction of the gravity field are possible. Therefore, it is assumed than the influence of gravity may be, in average, neglected. Centrifugal forces that may arise from the rotation of the particles are not accounted for in the model.

Combining Eqs. (25)–(27) with $(\theta_c = \theta) < 90^\circ$, the following expression for the imbibition velocity of the meniscus at height y of a single capillary of radius r_{pore} is obtained

$$y\frac{dy}{dt} = \frac{\sigma_l r_{pore}\cos\theta}{4\mu_l}. \tag{28}$$

Substituting Eq. (23) into Eq. (28) and solving for h, the following expression is obtained:

$$h_{imb} = h_0 - \frac{2}{3}\varepsilon_p\left(\frac{\sin\theta}{1-\cos\theta}\right)^2\left[\frac{1}{1-\cos\theta} - \frac{1}{3}\right]^{-1}\sqrt{\frac{\sigma_l\cos\theta r_{pore}}{8\mu_l}}t^{1/2} \tag{29}$$

Eq. (29) can be used to calculate the imbibition time t_{imb} needed for reducing the height of a droplet deposited on a porous particle of porosity ε_p from h_0 to h_{imb} as a function of contact angle, liquid surface tension and viscosity.

3. Experimental methods

3.1. Micro-scale experiments: penetration of liquid binder into porous particles

Before introducing the penetration micro-model described by Eq. (29) into the main agglomeration model, several imbibition experiments of liquid binder (aqueous solution of hydroxypropylmethylcellulose (HPMC), Pharmacoat® 606 from Shin-Etsu, Japan) on porous alumina particles were carried out. A complete characterization of the properties of HPMC solutions can be found in Nagai et al. (1997) and Aulton et al. (1997). For the context of this work it is important to point out that the density and surface tension of the solutions do not considerably vary with the solute mass percentage, but the binder viscosity increases strongly with the solute concentration. Eq. (27) shows that the reduction rate of the binder layer is, then, mainly governed by the binder viscosity μ_l.

The experiments consisted in single droplet deposition of HPMC solutions of different viscosities on porous alumina particles by means of a micropipette. The micropipette was calibrated to deliver droplets of $V_d = 0.4$ μl corresponding to an equivalent diameter of $d_d = 0.9$ mm. The experiments were performed at ambient conditions of $T_g = 23$ °C and $Y_g = 5$ g/kg. Since no closed chamber was used, the air velocity in the vicinity of the droplet was measured by a thermal anemometer. A value of approximately $u_0 = 0.1$ m/s was observed. The alumina particles have a diameter of $d_p = 2.8$–3 mm, a porosity of $\varepsilon_p = 0.75$ and a pore radius of $r_{pore} = 5$ nm (Kwapinski and Tsotsas, 2006). The experimental parameters are shown in Table 1. The imbibition process was recorded by a medium-speed camera, the frame sequence analyzed and the height of the deposited layer monitored with time.

3.2. Lab-scale agglomeration experiments

The solids used for the agglomeration trials were glass and alumina particles. Solid properties are listed in Table 2. The glass beads were supplied by Cerablast, Germany, and the alumina particles by Sasol, Germany. The number density q_0 and the cumulative size distribution Q_0 for both solids were obtained by a Camsizer 0135, Retsch Technologies, Germany. Fig. 2(a) and (b) show the size distribution and the appearance of glass and alumina particles, respectively. The average particle diameter $d_{p,0} = d_{50}$ was obtained from Q_0. The particle sphericity of both solids was also obtained by the Camsizer.

Regarding the restitution coefficient for glass, it is reported in literature that the actual value lies between 0.9 and 0.7 depending on glass composition, impact velocity and angle of impact (Utikar and Ranade, 2007; Sommerfeld and Huber, 1999). For the sake of simplicity, a value of 0.8 was taken. The value for alumina particles is reported by Antonyuk et al. (2007). The particle density was obtained from measured bed density with a porosity of $\varepsilon_{bed} = 0.4$. The obtained values were found to be in good agreement with typical from literature. The intraparticle porosity of alumina is reported by Kwapinski and Tsotsas (2006). The pore diameter for the alumina particles used in the agglomeration

Table 1
Experimental parameters for the droplet penetration investigation.

x_b (%)	σ_l (N/m)	ρ_l (kg/m^3)	μ_l (Pa s)
2	0.0466	1001.5	0.008
4	0.0464	1007.5	0.025
6	0.0461	1011.2	0.060

Table 2
Properties of the glass beads and alumina particles.

	Glass	Alumina
Particle average diameter, d_{50} (mm)	0.40	0.36
Particle sphericity, ψ (dimensionless)	0.97	0.94
Restitution coefficient, e (dimensionless)	0.80	0.60
Particle density, ρ_p (kg/m^3)	2400	1400
Liquid–solid contact angle, θ (deg)	40	60
Intraparticle porosity, ε_p (dimensionless)	0	0.75
Pore radius, r_{pore} (nm)	0	4

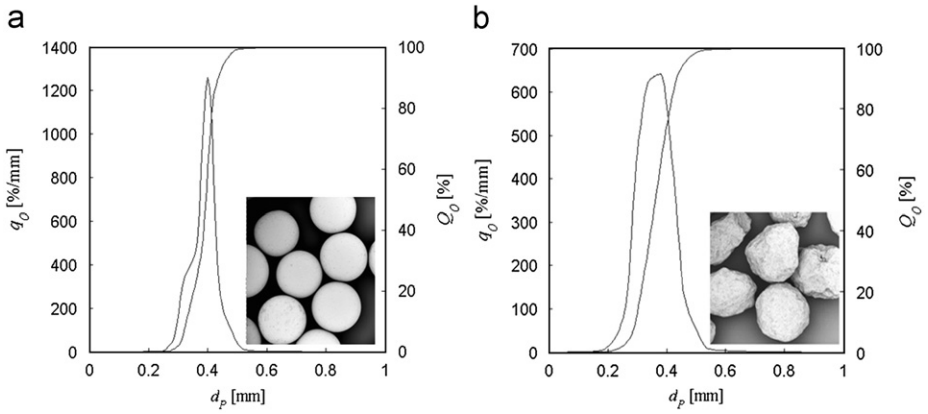

Fig. 2. Initial particle size distribution and appearance of glass (a) and alumina (b) particles.

experiments was determined by mercury intrusion. The contact angle for glass was obtained from droplet deposition experiments on glass surfaces (Terrazas-Velarde et al., 2009) and for alumina from the first frame of the droplet penetration experiments presented in Section 3.1. These values were found to be in accordance with experimental values reported in literature (Mao et al., 1997; Liechti et al., 1997; Chunsheng et al., 2008; Rendón et al., 2006).

The otherwise smooth surface of the glass particles had easily distinguishable asperities of approximately 10 μm in height. The surface of the alumina particles was rough. The height of the asperities of the alumina particles was difficult to estimate because the surface was irregular and asperities were present all over the surface with a widespread distribution of heights; well distinguishable asperities were usually located in depressions of the surface and they were quite long so that the distinction between an asperity and bigger irregularities could not be completely achieved. Then, the value of h_a for alumina particles was the result of the analysis of many SEM pictures of several particles. Sample pictures of both surfaces can be found in Terrazas-Velarde (2010).

The experiments were performed in a cylindrical lab-scale fluidized bed agglomerator with diameter of 15 cm and height 45 cm. The fluidization and atomization air was provided by gas dosing units. The binder was continuously added in top spray configuration by means of a two fluid nozzle from Schlick Series 970. The binder was the same as used for the investigation of the droplet penetration mechanism presented in the last section, HPMC. A piston pump controlled the binder addition rate and the online measurement of the sprayed amount was monitored by a balance. During agglomeration, samples were taken every 30 s; average diameter and particle size distributions were obtained by offline measurement using the Camsizer 0135, Retsch Technologies. The sampling was continued until bed defluidization. As binder viscosity has been identified to play a major role in the imbibition mechanism, variations of the initial binder composition were performed. The experimental parameters of the lab-scale investigation are shown in Table 3. The experiments are labeled E.01–E.06.

Unfortunately, the properties of the solid particles are so different that the porosity effect cannot be directly tested. Alumina particles are much lighter, so that under the same fluidization velocity the height of the alumina bed and its voidage will increase. This affects the travel distance of the droplets before they reach the bed and can produce significantly different droplet premature solidification rates. The binder–solid contact angle of both materials also differs. This leads to a situation in which the surface coverage of the droplets, as well as the initial deposited layer height are different, having a direct implication on the agglomeration behavior. In addition, alumina particles have higher asperities than the glass particles, and the restitution coefficients are also not the same. This makes the isolation of the imbibition mechanism in the lab-scale tests rather difficult, since no material differing only in its porosity but with otherwise identical properties is available.

Table 3
Lab-scale experimental parameters.

	Glass	Alumina
Bed mass, M_{bed} (g)	500	300
Particle average diameter, d_{50} (mm)	0.40	0.36
Particle density, ρ_p (kg/m^3)	2400	1400
Binder mass flow rate, $\dot{M}_l$ (g/h)	300	420
Fluidization velocity, u_0 (m/s)	1.35	0.78
Fluidization number, u_f (dimensionless)	8.5	10.3
Gas mass flow rate, $\dot{M}_g$ (kg/h)	100	58
Gas inlet moisture content, $Y_{g,in}$ (g/kg)	0.4	0.4
Gas inlet temperature, $T_{g,in}$ (°C)	30	30
Binder viscosity, μ_l (Pa s)	0.025 – 0.322	0.025 – 0.322
	4 (E.01)	4 (E.04)
Binder mass fraction, x_b (%)	8 (E.02)	8 (E.05)
	10 (E.03)	10 (E.06)

Nevertheless, the experimental process parameters were adjusted in such a way that the effect of the penetration mechanism could be indirectly tested. For example, in an attempt to reach approximately the same values for the height of the bed, the fluidization gas mass flow rate of the alumina experiments was reduced. Additionally, attention was paid to the comparability of parameters which are very important for model validation. One such parameter is the droplet addition rate γ. This quantity describes the number of droplets introduced to the agglomerator per primary particle and per second and is the base of the equivalence between the real and the simulated system (Eq. (1)). As this parameter varies with the number of primary particles and the binder addition rate, both quantities had to be modified for the case of alumina particles. The mass of particles was reduced to 300 g and the binder addition rate increased to 420 g/h. In this way, both systems show a value of $\gamma = 0.05\ s^{-1}$ (see Table 7 for the simulation parameters).

4. Results and discussion

4.1. Micro-scale experiments

Fig. 3 presents a typical sequence of the imbibition experiments performed in this study. It can be recognized that the

droplet penetrates into the porous substrate until it finally vanishes.

The experimentally obtained penetration times are shown in Fig. 4(a) as a function of binder viscosity and compared with the penetration model given by Eq. (29). As it can be seen, the model gives higher penetration velocities as the viscosity of the binder solution is reduced, which is also experimentally observed. However, the model underestimates the measured penetration velocity for every binder concentration. This underestimation becomes more severe as the binder viscosity increases. The reason of this behavior may be that droplets of low concentration penetrate, while droplets of high concentration additionally dry before they can fully go into the particles. This means, besides droplet penetration, drying of the deposited droplet also plays a role in the reduction of layer height. Then, the influence of drying is expected to be more pronounced for highly viscous binders. In order to implement this effect, the drying model described by Eq. (11) was used.

Fig. 4(b) plots the experimental results against the combination of both, the imbibition and the drying model. As it can be seen, the model comes significantly closer to the experimental results for all binder compositions when the drying mechanism is included. A part of the remaining derivation may be caused by the two parameter model equation used in the derivation of the imbibition model, specifically in Eq. (25), where a is substituted by h. The two parameter model (Eqs. (2) and (3)) is valid as long as $d_d \ll d_p$. Under these conditions, the particle curvature can be neglected and the geometrical relationships are very accurate. As the two diameters come closer, a progressive loss of accuracy is observed. The experiments of this study were performed at show a value of $d_p/d_d \approx 3$. For this aspect ratio and the experimental conditions, Eq. (3) gives an underestimation of approximately 20% of the actual value of h.

The assumption that both contact angles, surface and capillary, are equal and constant during imbibition represents an additional uncertainty as this may or not be the case. Another possible explanation for the deviations of the model may be found in the non-accounting of the centrifugal forces that may appear as the particles and the deposited droplets rotate within the fluidized bed. However, the main reason for the observed deviation is seen in the model assumption of equally sized, uniformly distributed straight and parallel capillaries. Fitting in the frame of this model is not necessary for the present investigation and would not make much sense. Thorough studies by means of pore network models (see, for example Metzger et al. (2007)) are planned for the future.

Irrespectively of the attained accuracy, even this simple model is sufficient to discuss conditions that lead to the clear conclusion that the porous character of the primary particles has a stronger influence at low binder viscosities since much more droplets will be lost due to penetration. This causes a significant reduction of the agglomeration efficiency of porous particles. On the contrary, at high viscosities, droplet penetration is impeded and a similar behavior between porous and non-porous particles is expected.

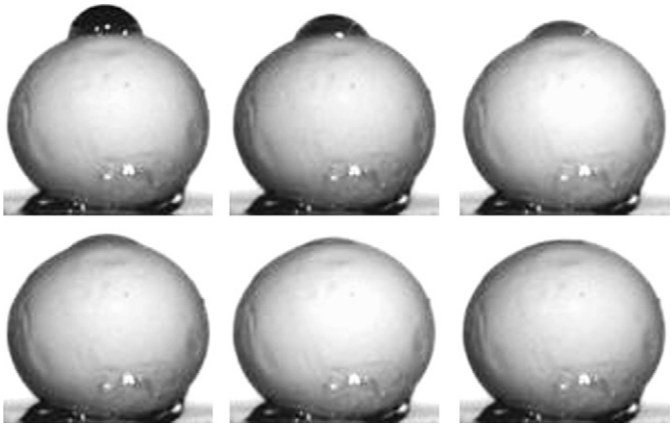

Fig. 3. Droplet penetration into a porous alumina particle.

4.2. Lab-scale agglomeration experiments

Fig. 5(a) and (b) show the experimental results for non-porous (glass) and porous (alumina) particles, respectively. In Table 4, the results are expressed as agglomeration rates R obtained by linear least squares regression over all the measured points. As it can be seen, for both systems, agglomeration rate is enhanced as binder viscosity increases. This is expected since a more viscous layer is able to dissipate a larger fraction of the collision energy resulting in a higher number of coalescence events. This tendency was already discussed in previous literature (Ennis, 1996; Tan et al., 2006; Terrazas-Velarde et al., 2009).

It can also be observed that even if the binder addition rate for alumina is almost 50% higher than the one for glass (recall that γ must be kept constant), the agglomeration rates of both systems for the same viscosity stays very close to each other (Table 4). This phenomenon contradicts the well proved theory that the binder addition rate determines the speed of agglomeration

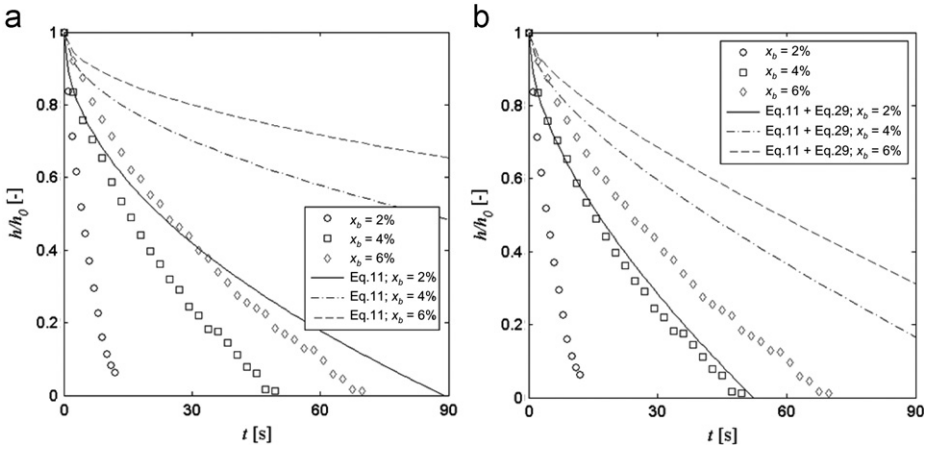

Fig. 4. Comparison of the pure imbibition model (a) and the combined drying–imbibition model (b) with measured droplet heights.

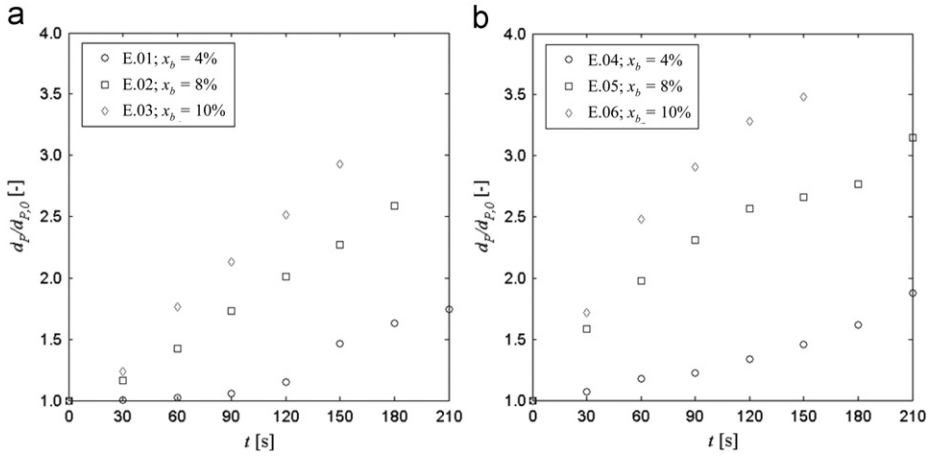

Fig. 5. Experimentally obtained change of particle size for glass beads (a) and alumina particles (b) as function of the initial binder mass percentage.

Table 4
Measured average agglomeration rates.

x_b (%)	R_{glass} (mm/s)	R_{alum} (mm/s)
4	0.0019	0.0022
8	0.0036	0.0035
10	0.0052	0.0060

Table 5
Initial agglomeration window $w=St^*_{coal,0}-St_{coal,0}$ for glass and alumina particles as function of asperities height h_a and binder mass percentage x_b.

h_a (mm)	w_{glass} (dimensionless)			w_{alum} (dimensionless)		
	4%	8%	10%	4%	8%	10%
0.010	−0.55	1.82	2.09	2.63	3.35	3.43
0.015	−1.47	0.90	1.17	1.55	2.27	2.35
0.020	−2.11	0.26	0.53	0.78	1.50	1.58
0.025	−2.62	−0.25	0.02	0.18	0.90	0.98

(Tan et al., 2006). Then, it would be expected that, under the given conditions, the alumina system agglomerates much faster than the glass particles. By looking at Table 3, it can also be noticed that the fluidization velocity for alumina is lower than the one used in the glass system (recall that the distance from the top of the bed to the tip of the nozzle should be kept constant). It is known that, in top-spray drying process with aqueous based binders, smaller fluidization velocities lead to higher agglomeration rates. However, even if the fluidization gas for alumina is approximately 50% smaller than the one for glass, the positive effect of lowering u_0 is not really seen in Fig. 5 or in Table 4. Then, it can be inferred that there is an additional phenomenon which hinders the alumina system from showing a much faster agglomeration, even if the binder addition rate is 50% higher and the fluidization velocity 50% lower than for glass particles.

Table 5 presents the calculated initial agglomeration window ($w=St^*_{coal,0}-St_{coal,0}$) for different values of surface asperities height h_a for both systems, glass and alumina particles, at the experimental conditions. The agglomeration window w is an indicator of the coalescence ability of the system. Large agglomeration windows exist when the Stokes number is far from the critical Stokes number. This eventually means that the system is allowed to grow within a larger operational range. Small agglomeration windows describe a system which is very close to its limiting, maximum coalescence size.

Table 6
Parameters for the calculation of $St_{coal,0}$ and $St^*_{coal,0}$. for glass and alumina systems.

	Glass	Alumina
e (dimensionless)	0.80	0.60
θ (deg)	40	60
h_0 (mm)	0.0279	0.0371
$M_{p,0}$ (g)	8.04×10^{-5}	3.44×10^{-5}
$d_{p,0}$ (mm)	0.40	0.36
u_c (m/s)	0.675	0.390

It is important to point out that the values of the agglomeration window are totally independent from the porous character of the materials and are calculated with the mean value of the collision velocity $u_c=0.5u_0$, droplet diameter $d_{d,0}=80$ μm and $h=h_0$ as given in Table 6. Additionally, it has to be said that the fact that other parameters than particle porosity were changed when switching from glass to alumina is already included in the parameter w, agglomeration window, for glass and alumina because for the calculation of w the experimental parameters are used.

As it can be seen, the agglomeration window for the alumina particles is significantly larger than the one for the glass particles at every binder viscosity and asperities height, therefore it is expected that the glass particles agglomerate much less. Particular attention deserves the lowest viscosity case for the non-porous system where a negative agglomeration window is observed. A value less than zero means that, initially, the Stokes number exceeds the agglomeration limit; under these conditions no size enlargement can take place. However, as the deposited droplets dry on the particles, they increase in viscosity and at some time the droplets are viscous enough to dissipate the collision kinetic energy and produce a successful coalescence. From this point on, agglomeration is possible. This can explain the initial non-growth period for the experiments with glass particles at the lowest initial viscosity (E.01) shown in Fig. 5(a).

It is obvious that the glass system, particularly at low binder viscosities, has a big disadvantage in comparison to the alumina system. The agglomeration window of glass must first reach the value of zero (when $St_{coal}\approx St^*_{coal}$) before the first coalescence can take place, while the alumina system starts size enlargement right after the binder is sprayed onto the bed. Moreover, even if the system overcomes this limit, the alumina agglomeration window is still much wider than the one observed for glass particles. Therefore, it is expected not only that alumina

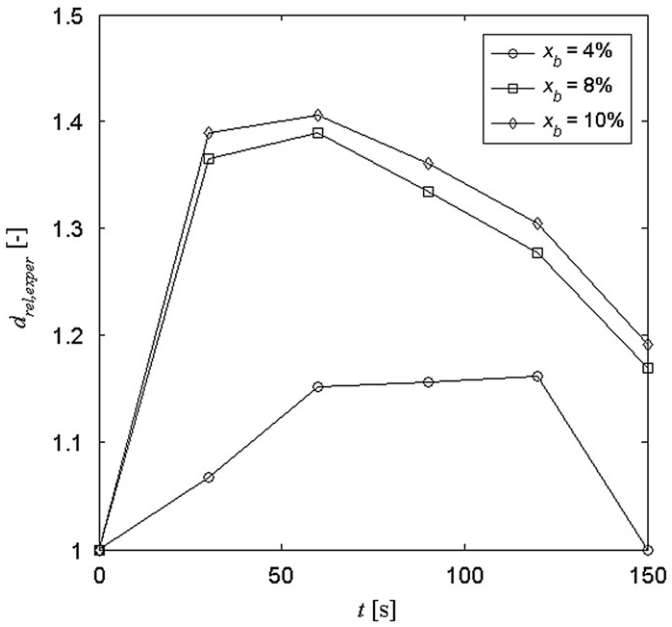

Fig. 6. Experimentally obtained relative diameter between alumina (PO) and glass (NP) particles.

agglomerates faster, but also that the difference between the two systems should be much higher at a binder mass percentage equal to 4%.

A useful representation of the experimental results is given in Fig. 6 by the diameter ratio between the porous and non-porous particles

$$d_{rel,\mathrm{exper}} = \frac{(d_p/d_{p,0})_{alum}}{(d_p/d_{p,0})_{glass}}. \tag{30}$$

There it can be recognized that, contrary to the expected response, the lowest difference ($d_{rel,exper}$ closest to unity) is observed for the lowest tested mass percentage of 4%. According to the above explanation, however, the lowest viscosity curve should lie above the other two lines, which is obviously not the case.

This clearly suggests that the negative effect of droplets lost due to binder imbibition into the porous particles, which is much stronger for low viscosity binders, has caused the reduction of the experimental agglomeration rate for porous particles. This negative effect was obviously big enough to overcome the main trend and even forced the curve under the other two lines. In order to demonstrate this interpretation, two main groups of simulations were performed, "real system" simulations for non-porous glass and porous alumina and "fictitious system" simulations which correspond to porous glass and non-porous alumina. In the porous cases, both systems are assumed to show the same porosity ε_p and pore radius r_{pore} as the alumina particles (Table 2).

4.3. Isolation of the droplet imbibition mechanism, simulation results

Due to the significantly different properties of the two solids, it was necessary to carry out two sets of simulations, one according to the glass properties and a second one following the alumina properties, each of the sets with and without particle internal porosity. The simulation parameters follow the experimental parameters given in Table 3. Additional parameter are as per Table 7. For the simulations, two important parameters should be additionally known, the height of the asperities h_a and the time between collisions, represented by the collision frequency pre-factor F_{coll}. The measurement of the height of the asperities for the alumina particles was, as stated before, a difficult task due to the irregular particle surface. However, as the agglomeration window w for glass is at any value of asperities height narrower than the one exhibited by the alumina system, and knowing that $h_{a,glass}$ is approximately 10 μm, a 50% higher value was assumed for the alumina particles ($h_{a,alum}$=15 μm).

Table 7
Simulation parameters.

	Glass	Alumina
h_a (μm)	10	15
d_d (μm)	80	80
γ (1/s)	0.05	0.05
T^* (°C)	14.0	17.8
$\tilde{y}_g$ (dimensionless)	0.0054	0.0122
Y_g (g/kg)	3.4	7.6
F_{coll} (1/m)	10	45
$f_{coll,0}$ (1/s)	1.6	4.1
$t_{step,0}$ (s)	0.625	0.244
$N_{p,0}$ (dimensionless)	2000	2000

Regarding the collision behavior of the systems, a suitable collision frequency pre-factor F_{coll} was obtained by adjusting the results of the non-porous (NP) simulation with x_b=8% to the corresponding experiment (E.02) for the glass particles. For the alumina system, the model predictions of the porous (PO) simulation with the highest tested binder concentration x_b=10% were adjusted to the experiment at the same conditions (E.06). This was done because it is expected that the effect of droplet imbibition is less strong for higher binder mass percentages and, therefore, the effect of the number of collisions can be better isolated than in the lower viscosity cases. The best fitting values were F_{coll}=10 for glass and F_{coll}=45 for alumina (see Table 7). A deeper discussion on the effect of the number of collisions in the agglomeration behavior can be found in Terrazas-Velarde (2010) and Terrazas-Velarde et al. (in press).

Fig. 7(a) and (b) present the comparison of simulation results between non-porous particles and their porous counterparts for glass and alumina systems, respectively. As it can be seen, the agglomeration rate is significantly decreased when the imbibition mechanism is implemented into the model. While in the non-porous simulations the droplets are lost only through drying, when imbibition is accounted the deposited droplets additionally penetrate into the porous substrate.

Fig. 8 depicts the relationship between the layer reduction velocity by imbibition and by drying as a function of the binder mass percentage for binder deposited on (fictitious) porous glass in the form

$$\upsilon = \frac{(dh/dt)_{imb}}{(dh/dt)_{dry}}. \tag{31}$$

Consequently, $\upsilon < 1$ represents conditions for which the layer reduction process is dominated by the drying mechanism. As it can be seen, low-viscosity droplets penetrate considerably faster and the aging of the layer is governed by penetration. For the high-viscosity cases, the penetration mechanism is not that important and the reduction of the layer results from a combination of both, drying and penetration.

Table 8 presents for both systems the time necessary to reduce the binder height h to the height of the asperities h_a, for pure drying and for the drying–imbibition model. The limit $h=h_a$ defines the minimum binder height that satisfies the first agglomeration condition. As it can be seen, the consideration of imbibition has a direct influence on the time period, during which

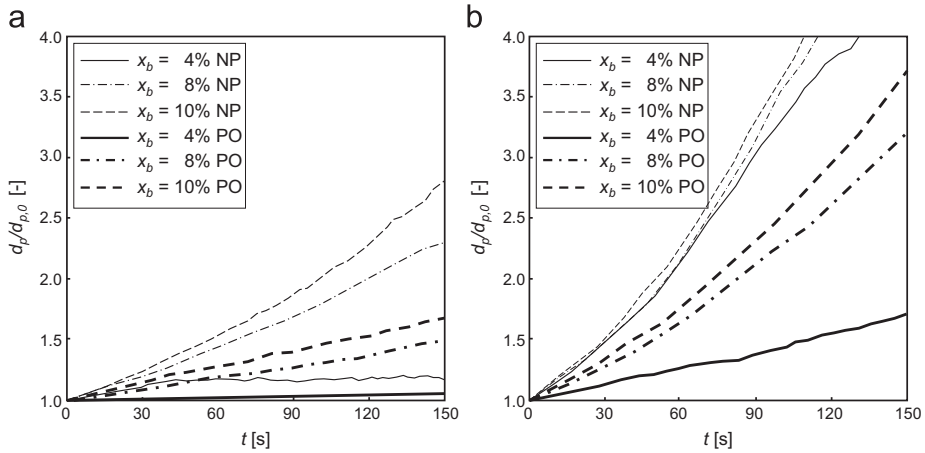

Fig. 7. Effect of the consideration of the imbibition mechanism (bold curves) for glass (a) and alumina (b) particles as function of the binder mass percentage.

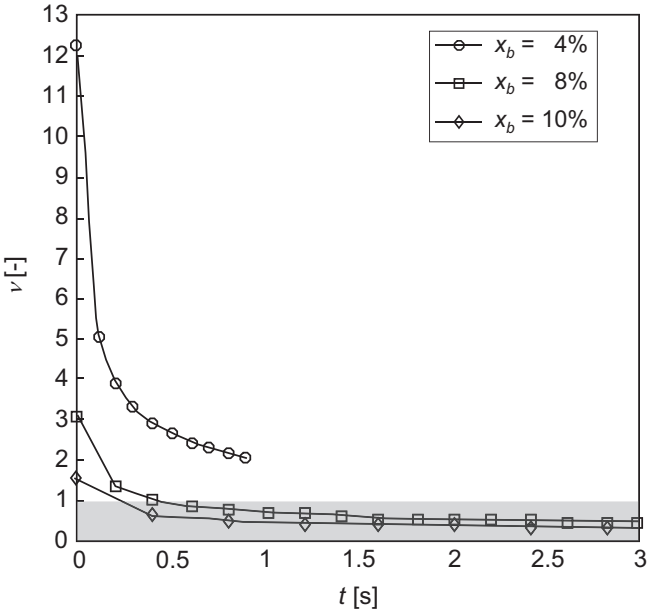

Fig. 8. Relative aging velocity by penetration and drying.

a droplet is able to form a bridge. An additional important parameter is the length of the interval between collisions. Table 8 additionally presents the number of collisions that a droplet can undergo before its maximum height becomes smaller than h_a. This value can be approximated to the integer function of

$$N_{coll,dry} = \frac{t_{dry}}{t_{step}} + 1, \tag{32}$$

for processes accounting only drying as a droplet aging mechanism, and

$$N_{coll,dry+imb} = \frac{t_{dry+imb}}{t_{step}} + 1, \tag{33}$$

when additionally intraparticle droplet penetration is considered. As the droplet can theoretically also be consumed immediately after deposition, the minimum possible value of N_{coll} is unity. Since the length of the time step varies in the course of the simulation, the calculated N_{coll} represents only an approximation. However, it gives a good indication of the number of collisions that a potentially usable droplet survives on the particle surface. When the imbibition mechanism is considered, the number of collisions in which a droplet can still be used is reduced. As expected, this reduction is much stronger for low viscosity binders due to the higher imbibition velocities. This has direct implications in the fulfillment of the agglomeration conditions.

Figs. 9 and 10 present the relative height of the deposited droplet at the moment of coalescence for both systems as a function of the initial binder concentration. It is easily recognizable that when imbibition is accounted less droplets produce a successful coalescence. Additionally, it is seen that the height of the consumed droplet is significantly influenced by the binder mass percentage. For the glass system and at low binder viscosity the droplet is able to dissipate the collision energy only immediately after deposition (fresh droplet) and solely when $u_c < 0.54$ m/s (condition at which $St_{coal} = St^*_{coal}$). Recall the initially negative value of $w_{glass} = -0.55$ for the glass system at $x_b = 4\%$ and $u_c = 0.675$ m/s shown in Table 5. However, as the collision velocity is a distributed quantity with $\sigma_{uc} = 0.1$ m/s, there is a probability of approximately 10% that the actual value lies under the critical collision velocity. Hence, coalescence is still possible after a wet collision. Such a small number of agglomeration events is responsible for the size enlargement of the "porous" glass particles at $x_b = 4\%$. When intraparticle droplet penetration does not occur, the droplet reduces in height, increases its viscosity and stays longer on the particle surface. Therefore, a more distributed pattern of droplet consumption is observed. As the initial binder viscosity increases, more droplets can be used for agglomeration even after they already have partially penetrated into the particle. Note that the droplet consumption shows a step-wise pattern which is a consequence of the event-driven nature of the method. In order to better explain this situation, we take Fig. 9(a) as an example. There, five lines of consumed droplets are seen. This is directly related to the maximum number of collisions that a droplet stays on the particle as long as $h/h_a > 1$. These five lines represent the properties of the droplets at the first, second, etc., until the fifth collision after their introduction to the system. By the time at which a sixth collision occurs, the droplets have already dried out and the wet zone has vanished. Hence, no sixth line of consumed droplets is observed.

A further comparison of these limiting cases is depicted in Fig. 11 as the relative diameter for real glass and fictitious non-porous alumina given by

$$d_{rel,sim} = \frac{(d_p/d_{p,0})_{alum,NP}}{(d_p/d_{p,0})_{glass,NP}}. \tag{34}$$

The highest relative difference between the materials is clearly seen for the lowest binder viscosity. Then, the agglomerate diameter of non-porous alumina is considerably larger than the agglomerate diameter of glass. When comparing with the experimental results, Fig. 11 with Fig. 6, it can be easily recognized that

Table 8
Characteristic drying time t_{dry} and drying–imbibition time $t_{dry,imb}$ at $h=h_a$, and number of collisions N_{coll} during the time period with $h > h_a$ as functions of the binder mass percentage.

x_b (%)	Glass				Alumina			
	t_{dry} (s)	$N_{coll,dry}$ (dimensionless)	$t_{dry+imb}$ (s)	$N_{coll,dry+imb}$ (dimensionless)	t_{dry} (s)	$N_{coll,dry}$ (dimensionless)	$t_{dry+imb}$ (s)	$N_{coll,dry+imb}$ (dimensionless)
4	2.4	5	0.36	1	3.8	16	0.82	4
8	2.4	5	1.00	2	3.8	16	1.92	9
10	2.4	5	1.32	3	3.8	16	2.38	11

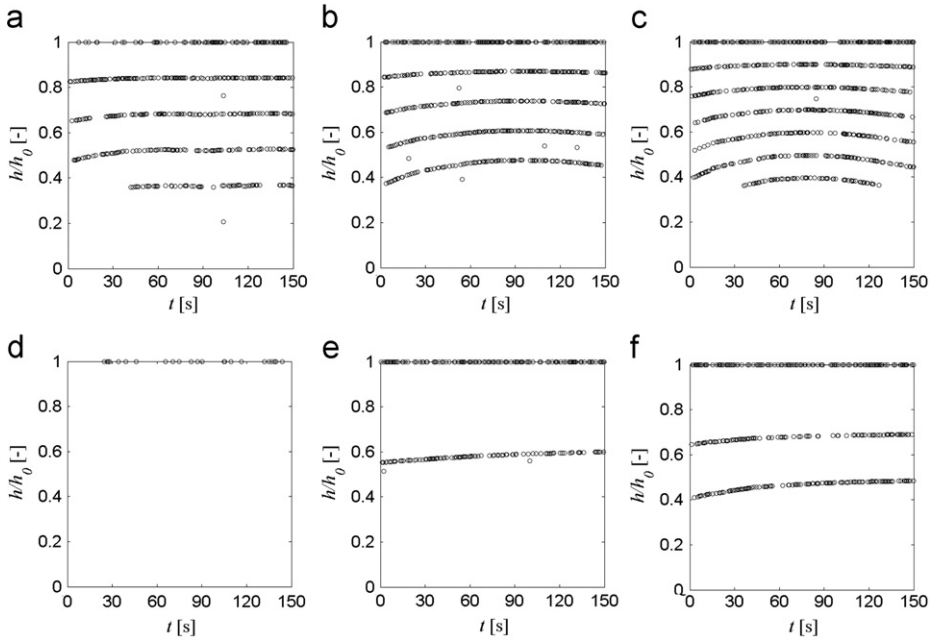

Fig. 9. Effect of the imbibition mechanism on the relative height of the deposited droplet at the exact time of coalescence as function of the binder mass percentage for glass particles.

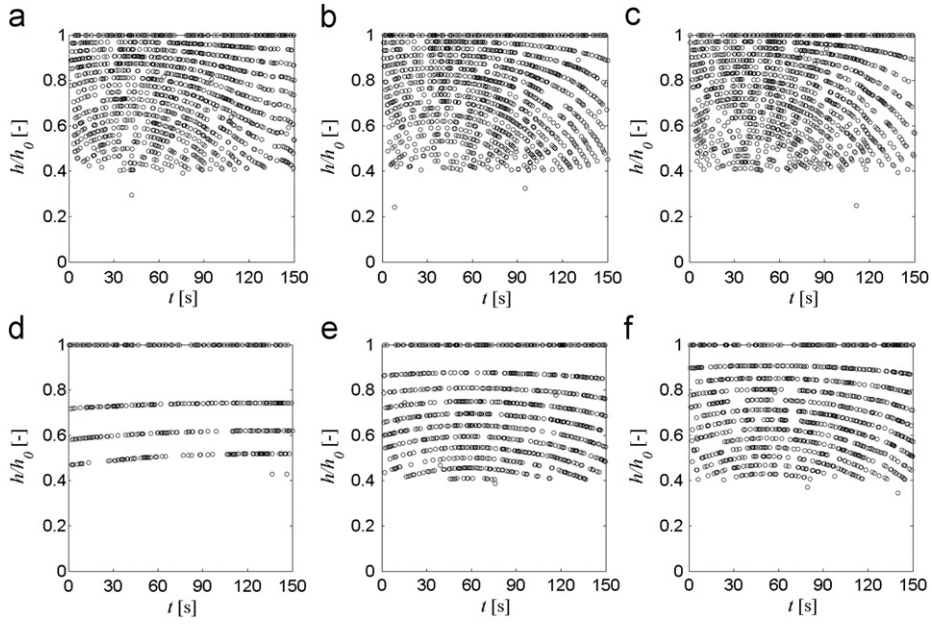

Fig. 10. Effect of the imbibition mechanism on the relative height of the deposited droplet at the exact time of coalescence as function of the binder mass percentage for alumina particles.

the general experimental tendencies are not conserved. This result corroborates that, under the given conditions and without accounting for the imbibition of droplets, the highest difference between the two systems would be observed at $x_b=4\%$, as it was explained before with the values of the initial agglomeration window w given in Table 5.

The extent at which the simulation results are affected by imbibition is further analyzed with the help of the real porous alumina simulations presented in Fig. 12 as

$$d_{rel,sim}=\frac{(d_p/d_{p,0})_{alum,PO}}{(d_p/d_{p,0})_{glass,NP}}. \tag{35}$$

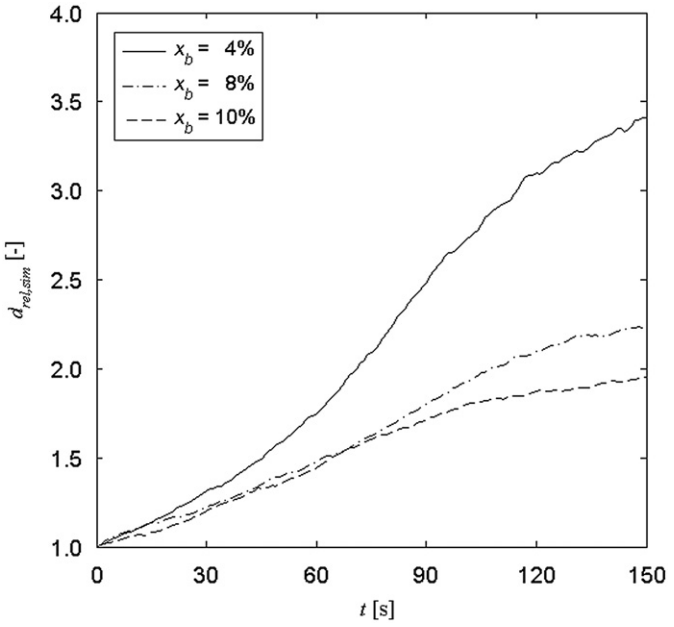

Fig. 11. Diameter ratio of fictitious non-porous alumina (NP) and non-porous glass (NP) particles, simulations.

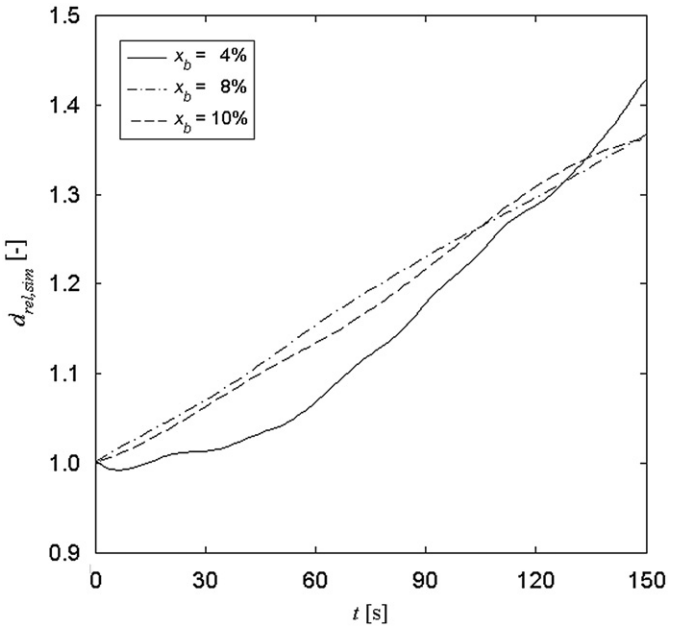

Fig. 12. Diameter ratio of real porous alumina (PO) and non-porous glass (NP) particles, simulations.

In this plot, analogous to Fig. 6 where experimental values of the same ratio are presented, it can be seen that by accounting the imbibition phenomenon, the smallest difference between the two systems occurs at the lowest binder concentration. This demonstrates that even if the fictitious alumina particles tend to agglomerate much faster than the glass beads, the consideration of the droplet loss due to imbibition reduces the real alumina agglomeration rate to an extent that both, glass and real alumina rates are close to each other. This corresponds much better to the experimentally observed tendencies presented in Fig. 6.

Fig. 13 gives a summary of the relationships between the simulation results for the four investigated systems of particles, real and fictitious, together with the experimentally obtained values as a function of initial binder viscosity. The results are presented as relative agglomeration rates R with respect to the corresponding highest agglomeration rate $R_{max,exper}$ obtained by the experiments ($x_b=10\%$). Then, for glass particles it is

$$\frac{R}{R_{max,exper}}=\frac{R_{glass,j}}{0.0052\,\mathrm{mm/s}}, \tag{36}$$

where j denotes the experiment (Exp. Glass), simulated non-porous glass (Sim. Glass NP) or simulated porous glass (Sim. Glass PO).

An analogous relationship for the alumina particles is given by

$$\frac{R}{R_{max,exper}}=\frac{R_{alum,j}}{0.0060\,\mathrm{mm/s}} \tag{37}$$

where j corresponds to the experimental alumina agglomeration rate (Exp. Alumina), simulated non-porous alumina (Sim. Alumina NP) or simulated porous alumina (Sim. Alumina PO). As it can be seen, the simulation of glass without imbibition and the simulation of alumina with imbibition are close to the experimental results. The artificial introduction of imbibition to glass leads to much smaller than the experimental agglomeration rates. On the contrary, much larger than the measured agglomeration rates are obtained when imbibition into alumina is suppressed. This indicates that the inclusion of the imbibition mechanism is indispensable when simulating substrates with internal porosity. The results also demonstrate that the effect of droplet penetration

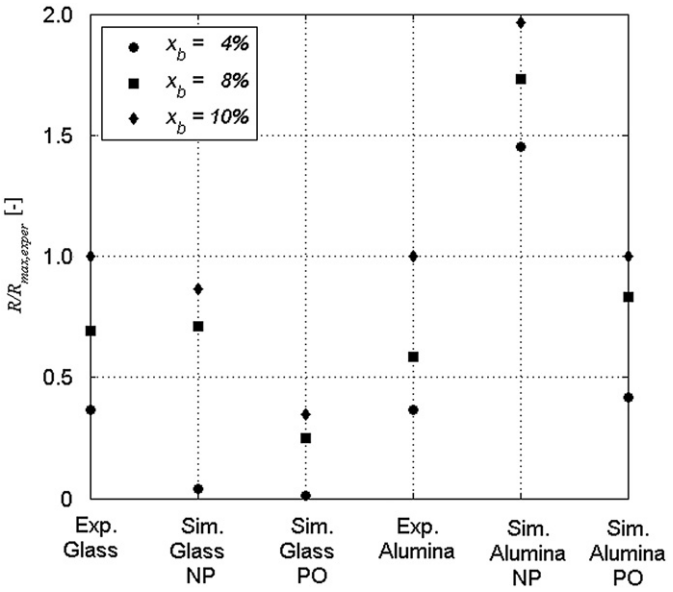

Fig. 13. Effect of imbibition at different binder mass percentages; comparison between simulations and experimentally obtained agglomeration rates.

is particularly important at low binder concentrations, due to the higher droplet penetration rate.

5. Conclusions

The effect of intraparticle porosity on the behavior during fluidized bed spray agglomeration has been analyzed in this study. This micro-scale experimental investigation revealed that the main parameter governing the penetration velocity is liquid viscosity. As the viscosity of the binder increases so does the penetration time and the influence of a second micro-mechanism, namely deposited droplet drying, becomes much more significant. A penetration model was developed with the help of the Washburn equation and the results were compared with single droplet penetration experiments in an attempt to validate the micro-model. In this respect, areas of improvement are particularly seen in the relaxation of some assumptions of the imbibition model regarding the geometry of the proposed pore network or the calculation of the internal contact angle within the capillaries. However, even this relatively simple version of the model is sufficient to follow the general tendencies and the order of magnitude of the penetration velocities. Therefore, it was, together with a previously developed and validated drying model, implemented into a comprehensive stochastic model that allows the simulation of the size enlargement process in a batch top-spray fluidized bed agglomerator.

Two sets of simulations were carried out. The first set corresponds to the "real system" of non-porous glass and porous alumina and the second to the "fictitious system" of porous glass and non-porous alumina. The simulation results show that when the penetration mechanism is neglected, the largest difference between the two non-porous systems is obtained at low binder viscosities. The experiments, however, show the opposite trend, which can only be obtained when the penetration mechanism is implemented. This leads to the conclusion that the imbibition phenomenon significantly reduces the agglomeration rate by the loss of droplets into the substrate. For processes at low binder concentrations this phenomenon cannot be neglected. The inclusion of the penetration mechanism is, thus, necessary for a reliable simulation of the agglomeration process of porous materials.

The stochastic approach has shown once more that it is a flexible and relatively easy method which can incorporate several micro-mechanisms simultaneously. However, for its long term development, a deeper study of fluidized bed flow dynamics, particle collision frequency and relative collision velocities is unavoidable.

6. Nomenclature

a	base radius of spherical cap (m)
A	area (m^2)
d	diameter (m)
e	restitution coefficient (dimensionless)
f_{coll}	collision frequency (1/s)
F	force (N)
F_{coll}	collision frequency pre-factor (1/m)
g	gravity (m^2/s)
h	binder layer thickness (m)
h_a	height of particle surface asperities (m)
i	colliding pair (dimensionless)
k	event (dimensionless)
M	mass (kg)
$\dot{M}$	mass flow rate (kg/s)
$\tilde{M}$	molecular weight (kg/kmol)
N	number (dimensionless)
$\dot{N}_d$	droplet flow rate (1/s)
N_p	number of particles in simulation box (dimensionless)
$\mathcal{N}$	number of doublings (dimensionless)
P	pressure (Pa)
P_v^*	saturation vapor pressure (Pa)
q_0	number density size distribution (1/m)
Q_0	number density cumulative particle size distribution (%)
r	radius (m)
R	Agglomeration rate (m/s)
St_{coal}	Stokes coalescence number (dimensionless)
St^*_{coal}	Stokes coalescence critical number (dimensionless)
t	time (s)
T	temperature (°C)
u_c	collision velocity (m/s)
u_0	fluidization gas velocity (m/s)
u_f	fluidization number (u_0/u_{mf}) (dimensionless)
u_{mf}	minimum fluidization velocity (m/s)
V	volume (m^3)
w	agglomeration window (dimensionless)
x_b	binder mass percentage (%)
$\tilde{y}_g$	molar fraction in the gas phase (dimensionless)
Y	moisture content (g/kg)

Greek letters

β	mass transfer coefficient (m/s)
γ	droplet addition rate (1/s)
ε	porosity (dimensionless)
θ	contact angle (deg)
μ	viscosity (Pa s)
υ	relative aging velocity (dimensionless)
ρ	density (kg/m^3)
σ_l	surface tension (N/m)
σ_{uc}	collision velocity standard deviation (m/s)
ϕ	solid volume fraction (dimensionless)
ψ	particle sphericity (dimensionless)

Subscripts

agg	agglomerate
ad	addition
b	solute
c	capillary
cap	spherical cap, deposited droplet
coal	coalescence
coll	collision
d	droplet
dry	drying
end	end, final
exp	expanded bed
exper	experimental
fix	fixed bed
g	gas
gr	gravity
imb	imbibition
in	inlet
max	maximum
p	particle
pore	pores
rel	relative
sim	simulation
v	viscous
w	water

0	initial
*	saturation

Abbreviations

HPMC	hydroxypropylmethylcellulose
dry	drying mechanism
imb	imbibition mechanism
MC	Monte Carlo
NP	non-porous
PO	porous

Acknowledgements

The first author acknowledges the financial support by CONACyT (Mexico) and DAAD (Germany). Experimental facilities have been funded by DFG (Germany), PE1423-1-1.

References

Antonyuk, S., Tomas, J., Heinrich, S., 2007. Breakage dynamics and probability of granules by impact: impact test and DEM simulation. In: Proceedings of the Third International Conference on Population Balance Modelling, Quebec, Canada, September 19–21.

Aulton, M., Twichell, A.M., Hogan, J.E., 1997. Physical properties of HPMC solutions and their role in the film coating process and the quality of the coated product. In: McGinity., J.W. (Ed.), Aqueous Polymeric Coating for Pharmaceutical Dosage Forms second ed. Marcel Dekker, New York.

Buffière, P., Moletta, R., 2000. Collision frequency and collisional particle pressure in three-phase fluidized beds. Chem. Eng. Sci. 55, 5555–5563.

Chunsheng, R., Dezhen, W., Younian, W., 2008. Grafting silane onto silicate glass surface treated by DBD in air. Plasma Sci. Technol. 10, 556–559.

Clarke, A., Blake, T.D., Carruthers, K., Woodward, A., 2002. Spreading and imbibition of liquid droplets on porous surfaces. Langmuir 18, 2980–2984.

Couper, J.R., Penney, W.R., Fair, J.R., Walas, S., 2010. Chemical Process Equipment: Selection and Design, second ed. Elsevier, USA.

Cryer, S.A., 1999. Modeling agglomeration processes in fluid-bed granulation. AIChE J. 45, 2069–2078.

Czachor, H., 2007. Applicability of the Washburn theory for determining the wetting angle of solids. Hydrol. Processes 21, 2239–2247.

Ennis, B., 1996. Agglomeration and size enlargement. Session summary paper. Powder Technol. 88, 203–225.

Ennis, B.J., Tardos, G., Pfeffer, R., 1991. A microlevel-based characterization of granulation phenomena. Powder Technol. 65, 257–272.

George, D.C., Johri, J., Goldfarb, D., 2008. Dependence of particle fluctuation velocity on gas flow, and particle diameter in gas fluidized beds for monodispersed spheres in the Geldart B and A fluidization regimes. Powder Technol. 182, 146–170.

Gidaspow, D., 1994. Multiphase Flow and Fluidization: Continuum and Kinetic Theory Descriptions. Academic Press, Boston.

Kumar, J., Peglow, M., Warnecke, M.G., Heinrich, S., 2008. An efficient numerical technique for solving population balance equation involving aggregation, breakage, growth and nucleation. Powder Technol. 182, 81–104.

Kwapinski, W., Tsotsas, E., 2006. Characterization of particulate materials in respect to drying. Drying Technol. 24, 1083–1092.

Liechti, K.M., Schnapp, S.T., Swadener, J.G., 1997. Contact angle and contact mechanics of a glass/epoxy interface. Int. J. Fracture 86, 361–374.

Litster, J., Ennis, B.J., 2004. The Science and Engineering of Granulation Processes. Kluwer Academic Publishers, The Netherlands.

Mao, T., Kuhn, D.C.S., Tran, H., 1997. Spread and rebound of liquid droplets upon impact on flat surfaces. AIChE J. 43, 2169–2179.

Metzger, T., Iravan, A., Tsotsas, E., 2007. Influence of pore structure on drying kinetics: a pore network study. AIChE J. 53, 3029–3041.

Nagai, T., Obara, S., Kokubo, H., Hoshi, N., 1997. Application of HPMC and HPMCAS to aqueous film coating of pharmaceutical dosage forms. In: McGinity., J.W. (Ed.), Aqueous Polymeric Coating for Pharmaceutical Dosage Forms second ed. Marcel Dekker, New York.

Rajniak, P., Stepanek, F., Dhanasekharan, K., Fan, R., Mancinelli, C., Chern, R.T., 2009. A combined experimental and computational study of wet granulation in a Wurster fluid bed granulator. Powder Technol. 189, 190–201.

Rendón, R., Vázquez-Olmos, A., Mata-Zamora, M.E., Ordóñez-Medrano, A., Rivera-Torres, F., Sangier, J.M., 2006. Contact angle studies on porous alumina. Rev. Adv. Mater. Sci. 11, 79–87.

Sommerfeld, M., Huber, N., 1999. Experimental analysis and modelling of particle–wall collisions. Int. J. Multiphase Flow 25, 1457–1489.

Tan, S., Salman, A.D., Hounslow, M.J., 2006. Kinetics of fludised bed melt granulation I: the effect of process variables. Chem. Eng. Sci. 61, 1585–1601.

Terrazas-Velarde, K., 2010. Monte Carlo simulation of fluidized bed spray agglomeration. Ph.D. Thesis, Otto von Guericke University of Magdeburg.

Terrazas-Velarde, K., Peglow, M., Tsotsas, E., 2009. Stochastic simulation of agglomerate formation in fluidized bed spray drying: a micro-scale approach. Chem. Eng. Sci. 64, 2631–2643.

Terrazas-Velarde, K., Peglow, M., Tsotsas, E., in press. Investigation of the kinetics of agglomeration based on stochastic methods. AIChE J, doi: 10.1002/aic/12506.

Thielmann, F., Naderi, M., Ansari, M., Stepanek, F., 2008. The effect of primary particle surface energy on agglomeration rate in fluidized bed wet granulation. Powder Technol. 181, 160–168.

Utikar, R.P., Ranade, V.V., 2007. Single jet fluidized beds: experiments and CFD simulations with glass and polypropylene particles. Chem. Eng. Sci. 62, 167–183.

Washburn, E.W., 1921. The dynamics of capillary flow. Phys. Rev. 17, 273–283.

Zaho, H., Maisels, A., Matsoukas, T., Zheng, C., 2007. Analysis of four Monte Carlo methods for the solution of population balances in dispersed systems. Powder Technol. 173, 38–50.